ADVANCED HEALTHCARE MATERIALS
www.advhealthmat.de

Development of Neural Cells and Spontaneous Neural Activities in Engineered Brain-Like Constructs for Transplantation

Ke Gai, Mengliu Yang, Wei Chen, Chenyujun Hu, Xiao Luo, Austin Smith, Caizhe Xu, Hefeng Zhang, Xiang Li, Wei Shi, Wei Sun, Feng Lin, and Yu Song**

Stem cell transplantation has demonstrated efficacy in treating neurological disorders by generating functional cells and secreting beneficial factors. However, challenges remain for current cell suspension injection therapy, including uncontrollable cell distribution, the potential for tumor formation, and limited ability to treat spatial defects. Therefore, implants with programmable cell development, tailored 3D structure, and functionalized biomaterials have the potential to both control cell distribution and reduce or heal spatial defects. Here, a biomimetic material system comprising gelatin, alginate, and fibrinogen has been developed for neural progenitor cell constructs using 3D printing. The resulting constructs exhibit excellent formability, stability, and developmental functions in vitro, as well as biocompatibility and integration into the hippocampus in vivo. The controllability, reproducibility, and material composition of the constructs show potential for use in personalized stem cell-based therapies for defective neurological disorders, neural development research, disease modeling, and organoid-derived intelligent systems.

1. Introduction

Stem cell transplantation therapy has become a competitive approach for treating various neurological disorders, including Parkinson's disease, multiple sclerosis, Alzheimer's disease, stroke, and epilepsy.[1–5] This therapy has also shown efficacy toward local function restoration and cognition improvements in both animal models and preliminary clinical trials. Transplanted stem cells differentiate into specific cell types, integrate into neural circuits, and secret necessary factors, all of which assist in the healing process.[5,6] Despite the benefits, challenges such as tumor formation and immune rejection, low rates of cell integration in physiological and pathological environments, limited control over the direction of cell differentiation, and difficulties in structural repair remain.[5,7,8] These limitations necessitate a customized 3D implant tailored to specific temporal and spatial requirements with controllable differentiation and functional biomaterials.

Given the importance of controlled cell differentiation for successful implantation, it is imperative to select the correct cell type. Researchers have explored and validated arrange of dissociated stem cells for their applications in neural disorder treatment, including embryonic stem cells (ESCs), induced pluripotent stem cells (iPSCs), neural stem cells (NSCs), and mesenchymal stem cells (MSCs).[5] ESCs and iPSCs have the potential for personalized and versatile treatments, but ESCs are limited by ethical concerns, and iPSCs by tumorigenic risks. Meanwhile, MSCs and NSCs provide low immunogenicity and regenerative benefits but are difficult to acquire and have low pluripotency.[9,10] Hence, a promising approach is to use iPSC-derived neural progenitor cells (NPCs), which combine the benefits of iPSCs with the controllable differentiation of NSCs. 2D stem cell cultures provide well-defined, stable, and scalable transplants.[11–13] However, the ability of 2D cultures to integrate effectively and repair 3D structural defects is limited. In contrast, 3D organoids have exhibited improved ability to repair 3D defects[14–16] and demonstrated good vascular and neural circuit integration with host tissue in various animal models.[17–19] Nevertheless, 3D organoids face problems related to cell type, cell distribution, consistency, and shape manipulation.[20] Additionally, although self-assembling strategies mimic natural development, they lack controllability. Biomaterials are key factors in 3D constructs and are beneficial to the survival of implanted stem cells.[21] Functionalized biomaterials create a favorable microenvironment for transplanted cells by providing oxygen, ameliorating local inflammation, reducing glial fiber formation, and minimizing scarring.[22–25] Biomaterials also shield cells from stress-related damage, modulate cell differentiation, and facilitate the integration of transplanted

K. Gai, W. Chen, C. Hu, X. Luo, A. Smith, C. Xu, H. Zhang, X. Li, W. Sun, F. Lin, Y. Song
Biomanufacturing Center, Department of Mechanical Engineering
Tsinghua University
Beijing 100084, China
E-mail: linfeng@mail.tsinghua.edu.cn; y-song@mail.tsinghua.edu.cn
M. Yang, W. Shi
Beijing Advanced Innovation Centre for Biomedical Engineering, School of Engineering Medicine
Beihang University
Beijing 100084, China

The ORCID identification number(s) for the author(s) of this article can be found under https://doi.org/10.1002/adhm.202401419

DOI: 10.1002/adhm.202401419

cells.[26,27] In general, a precise and reliable method for producing patient-specific customized 3D implants is essential for advancing stem cell therapy.

3D bioprinting has been utilized to automate the construction and ensure the controlled distribution of cells and materials.[28–30] However, developing soft brain constructs presents significant material challenges. The low mechanical strength of suitable biomaterials for neural cells makes developing large 3D constructs difficult. Also, the biocompatibility of the biomaterials must be high enough to sustain long-term culture.[31–33] The introduction of new materials such as fibrinogen, gellan gum, and carboxymethyl cellulose (CMC) facilitates the fabrication of neural constructs[34–37] by providing biocompatible 3D environments closely resembling natural conditions. Furthermore, NSCs have been successfully printed to form functional brain constructs and implants[34,38–40] by employing new methods such as molecular cleavage[41] and droplet printing.[8] Despite these advances, there are still limitations in z-direction formation and geometric stability.[38,42] Lastly, 3D-printed brain-like constructs with developmental functions have not been well investigated for use as in vivo implants.

The objectives of this study were to firstly, develop a biomimetic material system suitable for bioprinting 3D neural constructs with z-direction formability; secondly, evaluate the in vitro developmental capacity of these constructs, including neurogenesis and neural differentiation; and lastly, assess the in vivo integration and functionality of these constructs in rat models. First, a biomimetic material system composed of gelatin, sodium alginate, and fibrinogen was developed to match the elastic modulus of brain tissue while providing formability, biocompatibility, and adjustability for extended in vitro cultures. Then, the material system and hiPSC-derived NPCs were utilized to fabricate an in vitro 3D construct that mirrors crucial early cerebral cortex development stages such as neurogenesis, neural differentiation, and maturation. The developmental capabilities of 3D constructs were experimentally verified. Next, constructs were implanted into the hippocampi of newborn rats for 34 days. The reproducibility and controllability of the construct make it promising for use in enhanced customized stem cell implants, neural development and disease modeling, and organoid-based intelligence systems (**Figure 1**).

2. Results

2.1. The Stability of Constructs Benefits the Development Models in Long-Term In Vitro Culturing and In Vivo Implantation

The constructs were designed with a grid pattern to facilitate the transfer of nutrients and oxygen to cells during long-term in vitro culture (Figure S1a and Code S1, Supporting Information). Without vascular components, the transfer of nutrients and oxygen was different from the in vivo diffusion condition post-implantation. Despite this, our grid structure aimed to partially mimic vascular function, with filaments of 600 µm in diameter and midline spacing of 1200 µm. Previous studies showed that 600–1000 µm diameter organoids survive and integrate well in rat brains,[18,43] suggesting our 600 µm structures should allow sufficient oxygen and nutrient access for cell survival. Insufficient transport of oxygen or nutrients across the construct results in lowered cell viability and eventual cell death. In addition, the stability and consistency of the constructs throughout the culturing procedure are vital for practical applications. Therefore, materials were selected to ensure construct printability, structural integrity, and long-term stability. Gelatin was chosen for its temperature-sensitive crosslinking, making it suitable for extrusion printing. Sodium alginate was chosen for its ability to solidify rapidly upon contact with calcium ions. Fibrinogen provides cell-adhesive peptides and long-term scaffolding for cells when augmented with aprotinin. The temperature sensitivity of the materials significantly influences the printing process. Temperatures below 11 °C resulted in over-crosslinking where the materials twisted and clumped together resulting in uneven printing. However, above 23 °C under-crosslinking occurred and the bioink remained liquid and formed droplets at the needle tips (**Figure 2**a,c; Figure S2a-i, Supporting Information). Rheological testing revealed a theoretical optimal gel-sol transition temperature of 20.08±0.94 °C (Figure 2d; Figure S2j-n, Supporting Information). Considering the heat exchange between the needle and its surroundings, the set temperature is 15 °C, and the printed constructs exhibited good shape fidelity under this condition (Figure 2b). The influence of different extrusion speeds on printing results was investigated at 15 °C, and 1.00 $mm^3 \cdot s^{-1}$ was selected as the extrusion speed. Clear grids, proper line diameter, and designed height were achieved using the selected parameters (Figure S3, Supporting Information).

During subsequent culturing the crosslinked materials were tested for physical and chemical stability. The elastic modulus of the constructs initially increased, then decreased, and eventually stabilized at ≈7.14 ± 1.46 kPa. All samples from different time points had an elastic modulus comparable to human brain tissue of between 3 and 10 kPa (Figure 2e). The range of elastic moduli observed across different time points suggests that the bioink created a physiological environment akin to in vivo conditions. Next, cells were introduced to the bioink. The interaction of the cells with the bioink caused a significant decrease in the elastic modulus after DAY 7 compared to the pure material group. However, the overall trend was the same in that they both increased first and then decreased, and the range was maintained between 3 and 7 kPa (Figure S4, Supporting Information).

The Fourier transform infrared spectroscopy (FTIR) showed a similar fingerprint region (red rectangle area) in the absorption spectrum of samples from DAYS 0 to 14 (Figure 2e). The FTIR results indicated minimal variation in the chemical composition of the constructs throughout the culture procedure. The results for sodium alginate showed peaks at 1032 nm, 1430 nm, and 1610 nm. The peak at 1032 nm was caused by the stretching vibration of the ether bond (-O-) on the calcium ion salt bridge. The peaks at 1430 nm and 1610 nm were caused by asymmetric vibration and symmetric stretching vibration of the carboxyl group. The absorption spectra of the constructs matched closely with that of alginate within the fingerprint region, confirming the presence of alginate throughout the culture period. Fibrinogen showed two peaks at 1616 nm and 1638 nm from the secondary bending vibration of the amine group (NH) (amide II band) and C = O stretching (amide I band). Gelatin also had peaks at 1598 nm for amide I and 1653 nm for amide II bands. The superposition of fibrinogen with gelatin resulted in broadening and offsets of the peaks corresponding to 1545 nm and 1655 nm in the

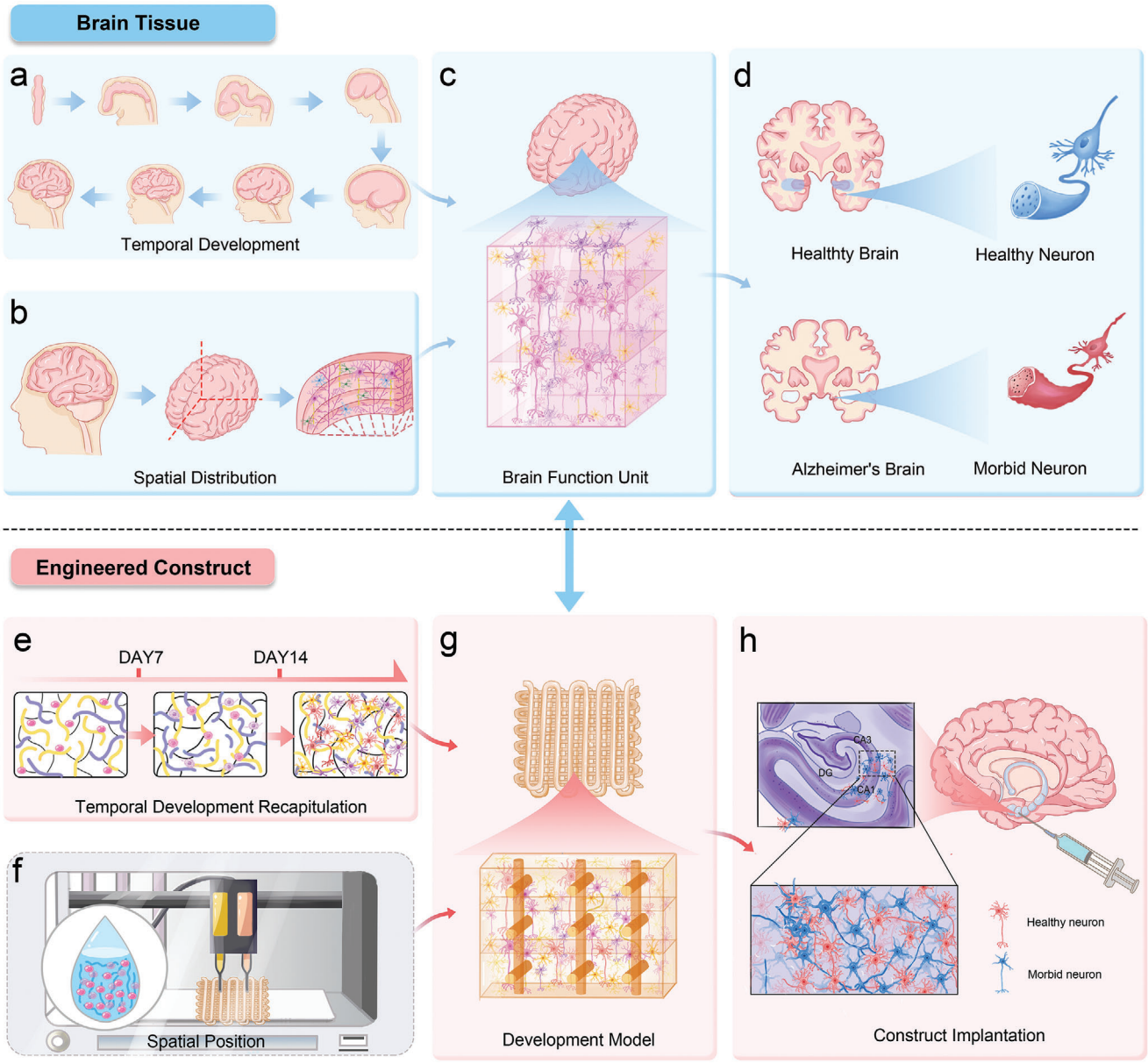

Figure 1. Fabrication of the engineered brain-like constructs with developmental capacity for implants. a-d Human brain development and disfunction. e-h) Construction and downstream applications of bioprinted cerebral construct corresponding to a-d. a) Development of human brain. b) Spatial distribution of cells within the human brain. c) Basic function unit of human brain, which is still being heavily studied. d) Healthy and diseased human brains with healthy and morbid cells. e) In vitro temporal recapitulation of human brain development using a biomimetic material system with programmed long-term culture with different media. f) 3D printing used to control the distribution of cells and materials. g) Through temporal and spatial control, a well-defined brain-like construct with the developmental ability to simulate crucial stages of early cerebral cortex development, including neurogenesis, neural differentiation, and neural maturation was established. h) Concept diagram of construct implantation treatments for diseases such as Alzheimer's disease and epilepsy.

hybrid material. In addition, the persistence of the peak at 848 nm throughout long-term incubation verifies the presence of gelatin. Although the absorbance of the samples changed as the incubation proceeded, the characteristic peaks did not disappear, and the relative height of each absorption peak did not change significantly. The results indicated that there was little variation in the ratio of gelatin to fibrinogen to alginate over the culture period. The corresponding characteristic peaks of each component of the cell-containing bioink persisted throughout the two-week incubation period, indicating that they were retained in proportion. However, the overall peaks of the cell-containing bioink were significantly higher and exhibited a trend of decreasing peaks with increased incubation time (Figure S5, Supporting Information). This trend suggested that intracellular proteins contributed to the amide peaks and material degradation was more pronounced in the presence of cells.

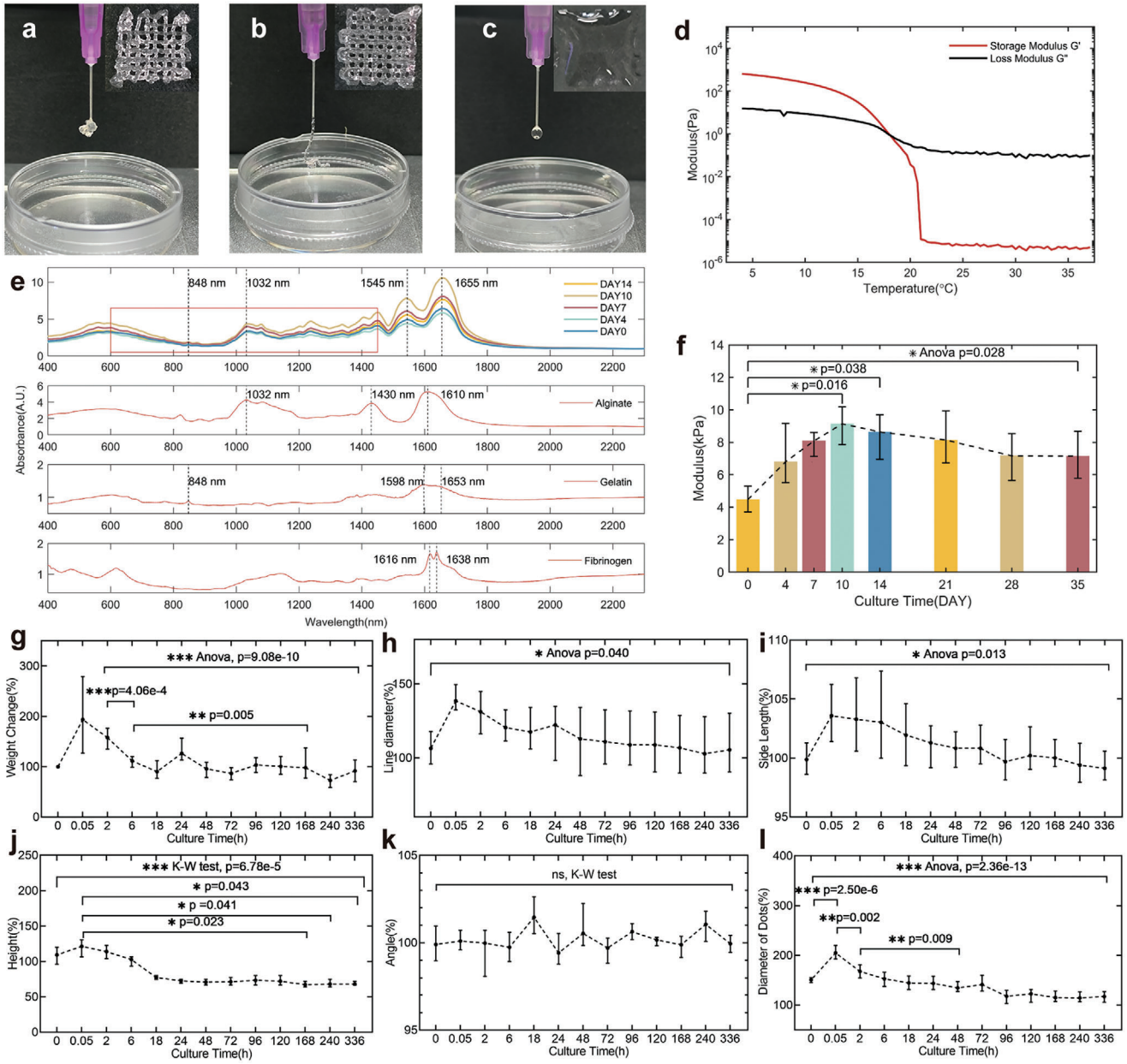

Figure 2. Basic mechanical and chemical properties of the bioink. a) Over-crosslinked bioink (9 °C). b) Properly crosslinked bioink (15 °C). c) Under-crosslinked bioink (25 °C). d) Rheological properties of the bioink. The intersection of the storage modulus and loss modulus curves was considered to be the gel-sol transition point of the bioink, the theoretical optimal printing temperature. e) FTIR results of constructs during two-week culture. 600 nm –1450 nm in the red frame was the fingerprint region. Pure gelatin, alginate, and fibrinogen groups were shown as references. f) Elastic modulus of crosslinked materials during 35-day culture procedure. ($n = 3$) Data presented as mean with range. An ANOVA test and corrected Tukey's multiple comparisons were applied to examine differences among groups of different dates. g) Degradation test of material over two weeks. ($n = 5$) Differences among groups after crosslinking (2 h) were examined using an ANOVA test and corrected multiple comparisons. h-k) Line diameters, side lengths, heights, and angle of printed grid constructs compared to designed parameters: diameter 600 µm, side length 10 000 µm, angle 90°, and height 750 µm. ($n = 4$) l) Diameters of dot constructs compared to the designed parameter of 1000 µm. ($n = 4$) Data presented as mean with range. Differences among groups within two weeks were examined using ANOVA tests and corrected multiple comparisons. Angles were analyzed with a K-W test and Dunn's multiple comparisons for non-normal distribution. *$p < 0.05$, **$p < 0.01$, and ***$p < 0.001$.

The degradation performance and fidelity of the constructs were tested in an artificial cerebral spinal fluid (aCSF) culture environment to mimic the in vivo brain environment. The hydrogel system rapidly expanded (within 3 min) and then slowly degraded and reduced to 102.19±16.22% of its original mass on DAY 14 (Figure 2g; Figure S6, Supporting Information). The results demonstrated the hydrogel was able to protect and hold cells in vitro for long-term culture. No significant difference was observed in the angle of the grid construct compared to the designed angle during the two-week culture period. The angle

was 99.95±0.36% of the designed angle at 336 h. Although the ANOVA test indicated significant differences among groups regarding line diameter and side length, no differences between groups were identified throughout multiple comparisons. Furthermore, the line diameters and side lengths were close to the designed parameters (105.46±15.13% and 99.14±0.91%, respectively) at 336 h. The height of the grid construct exhibited a significant decrease over the culture period. At 336 h, the height was 68.00 ± 2.31% of the designed value. In general, the shape fidelity of the grid construct was high (Figure 2h-k). However, the size of the dot construct reached the minimum resolution limit of the fabrication method at a diameter of 1 mm, and there was a significant discrepancy in shape fidelity compared to the grid construct (Figure 2l).

2.2. Proliferation and Differentiation of Neural Stem Cells Observed within Constructs

The constructs were cultured for at least two weeks after printing to evaluate cell proliferation and differentiation. Live/dead staining was conducted on DAYS 1, 7, 10, 14, and 130 to determine the live cell percentages in the constructs post-printing and during the culture process (**Figure 3**a–f). The live cell percentages increased post-printing but decreased from DAY 10 to DAY 14 (Figure 3g). Moreover, the live/dead images revealed that the cells gradually elongated within the constructs starting from DAY 4. The decrease from DAY 10 to DAY 14 suggests the occurrence of new cell deaths during the culture, with proliferation less rapid than in 2D culture conditions (doubling in a week). Furthermore, the viability of cells in 3D constructs was slightly lower in comparison to 2D cultures (Figure S7a-e,k, Supporting Information). However, in cultures exceeding 100 DAYS, a significant presence of live cells was observed, implying either consistent slow proliferation (aligning with in vivo self-repair) or a low average death rate over the long-term culture. Additionally, live cells were predominantly identified in regions where the bulk material was 100–300 µm thick, while dead cells were mostly in areas thicker than 500 µm. The reduced viability in thicker regions suggests the current material system may need to be more permeable to improve nutrient and oxygen transport. The distributions of live and dead cells in the whole construct were illustrated in Figure S7f-j (Supporting Information).

A stemness-maintenance culture medium was used for one week with daily medium changes to assess the differentiation potential of NPCs within the constructs. From the second week onward, a long-term culture medium based on Neurobasal Medium was applied every three days to remove the stemness-maintenance environment established by biochemical factors. The constructs were hydrolyzed at specific time points, and the extracted cells were analyzed for GFAP, Nestin, and NeuN expression via flow cytometry. In mammalian central nervous systems, NPCs generate neurons and astrocytes (Figure 3h), identifiable by NeuN and GFAP, respectively.[43] Throughout the procedure, approximately 80% of live cells expressed NeuN, while ≈20% expressed GFAP, indicating a rapid differentiation toward neurons rather than astrocytes after the stemness-maintenance environment was removed (Figure 3i). The total number of cells per construct was determined by digesting the constructs on DAYS 7, 14, 21, and 28, and the proliferation of each cell type during the entire culture process was hypothesized (Figure S7l, m, Supporting Information). The initial percentage of cells expressing NeuN was high but decreased over time, whereas GFAP expression was low but increased over time. This result suggested an early preference for differentiation toward neurons, followed by an increased differentiation toward astrocytes, consistent with developmental evidence from the mouse neocortex and human cortex.[44,45] However, in vivo embryonic neural genesis predominantly produces neurons from E10 to E17 and glial cells from E17 onward. Therefore, the culture period did not replicate the developmental process before E17 but resembled the postnatal development period. The rapid decline in the ratio of cells expressing NeuN to those expressing GFAP indicated a shift from neuron genesis to glia genesis. The gradual increase in the ratio of cells expressing NeuN to those expressing Nestin suggested a decline in the proportion of NPCs in the system over time, aligning with the in vivo developmental process (Figure 3j).

The flowcytometry results showed the proportions of different cell types in the culture system, yet their spatial distribution remained unclear. Hence, the distribution of different cell types was elucidated by immunofluorescent staining within the constructs. As illustrated in Figure 3k, on DAY 7, most of the cells inside the constructs were Nestin-positive, with only a few cells at the edge expressing NeuN. In comparison, for 2D cultures, more cells were slightly NeuN-positive, alongside a significant presence of Nestin-positive cells. In contrast, by DAY 14, an increased number of cells within the constructs expressed NeuN, indicating spontaneous in situ differentiation in the absence of a stemness-maintenance environment (Figure 3l). Although numerous cells continued to express Nestin, the fluorescence intensity diminished, suggesting a reduction in stemness. Similarly, under 2D culture conditions, only a few Nestin-positive cells remained, and most cells were NeuN-positive on DAY 14. The comparison between the 3D and 2D cultures highlighted that the 3D culture environment provided by the material substantially supported the maintenance of NPC stemness. Cells retaining stemness tended to remain inside the constructs, achieving an even distribution throughout. Moreover, without the stemness maintenance condition, NPCs in 3D culture could differentiate into neurons similar to those in 2D environments.

In conclusion, NPCs within constructs could proliferate, maintain stemness in the presence of biochemical factors, and differentiate spontaneously. This self-differentiation process aligned closely with the in vivo neural developmental process following birth.

2.3. Functional Neural Network Formation during Development

The survival and differentiation of cells within the constructs were demonstrated in previous sections to emphasize the developmental function of the construct. Neurite growth, calcium signaling, and electrophysiological functions of the cells were examined to further study developmental functions within the construct.

β-tubulin-iii, prevalent in neuron cell bodies, dendrites, axons, and axonal terminals, played a significant role in nervous system development and axonal transport. Neurite development served

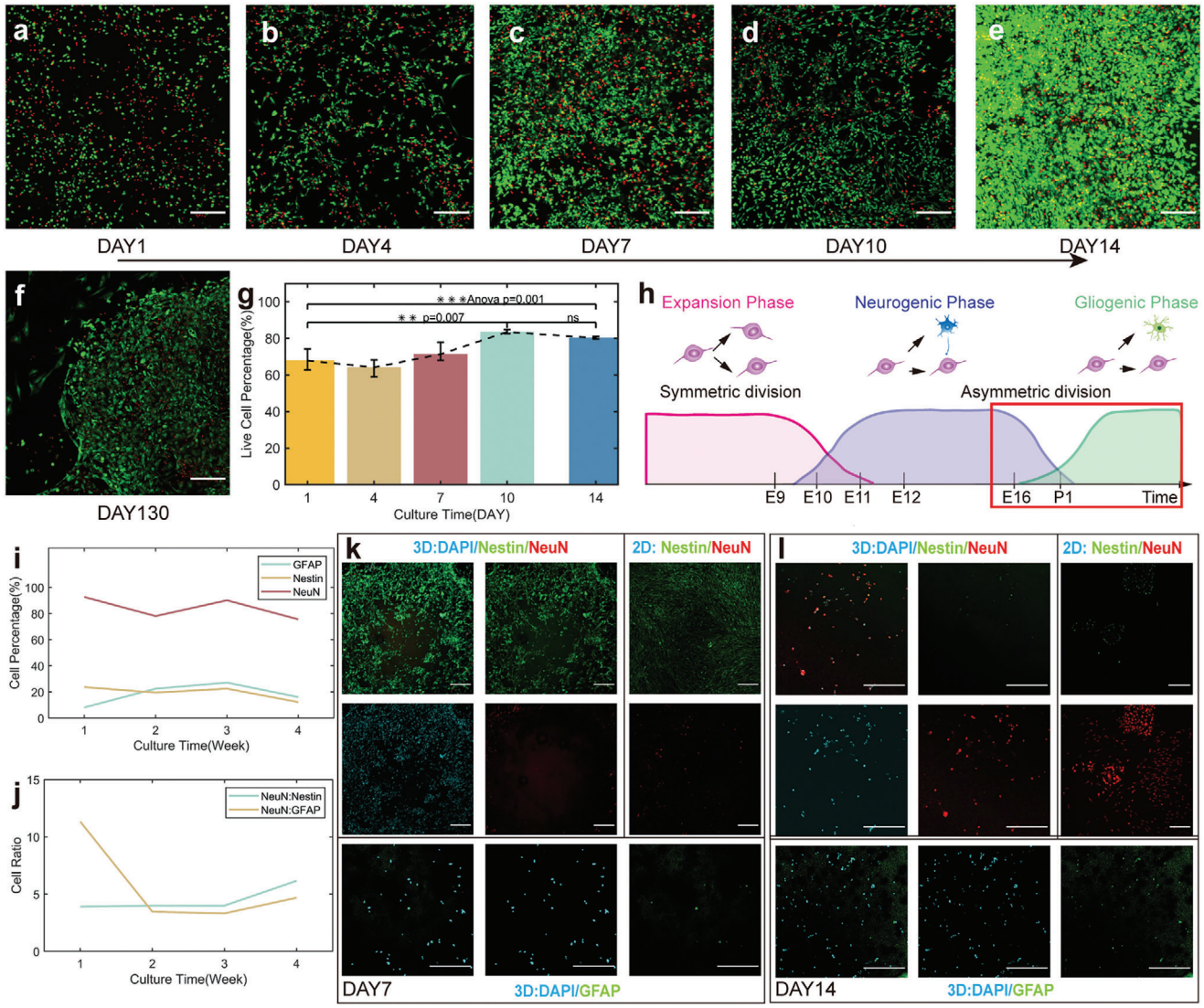

Figure 3. NPCs within constructs could proliferate and differentiate in situ. a–e) Live (green)/dead (red) images on DAYS 1, 4, 7, 10, and 14 are shown, respectively. Scale bar, 200 μm. f) Live (green)/dead (red) images of constructs undergoing a culture period of 130 days. Scale bar, 200 μm. g) Live cell percentages of constructs on DAYS 1, 4, 7, 10, and 14. ($n = 3$) A t-test was applied to examine differences between groups of different dates. *$p <$ 0.05, **$p < 0.01$, and ***$p < 0.001$. h) Developmental process of mammalian cortical cells. The time-line was set according to data extracted from the mouse. i) Percentages of cells with GFAP, Nestin, and NeuN during the 4-week culture according to flowcytometry analysis. In each week, samples were extracted at > or = to two time points and made into one data pool. j) Ratios of cells with NeuN to ones with Nestin and cells with NeuN to ones with GFAP during the 4-week culture according to flowcytometry analysis. The data were obtained using the same method as i. k, l) Immunofluorescence results of constructs and 2D cultures on DAYS 7 and 14. Red, green, and blue refer to NeuN, Nestin, and DAPI, respectively. GFAP was shown separately in green. Scale bar, 200 μm.

as a marker for brain tissue maturation. Therefore, β-tubulin-iii staining was employed to monitor neurite growth within the constructs. As depicted in **Figure** 4a–d, from DAYS 7 to 23, the number of neurites within the constructs steadily increased. On DAY 13, connections were observed only between cells within 80 μm of each other. However, beyond DAY 19, certain cells extended and formed connections with more distant cells. In the early stages of culture, a cell typically sprouted one or two neurites in almost vertical directions. Over time, as the culture period extended, a single cell could develop more than three neurites of varying lengths and orientations. Although many neurites were observed in cultures extending beyond one month, the material noise increased, decreasing the signal-to-noise ratio (SNR) and complicating the identification of neurite edges (Figure 4e). Consequently, neurite length data were collected and analyzed only for constructs within a one-month period, as shown in Figure 4f–h. An increase in neurite length enhanced neural network formation. In the first week, numerous neurites were approximately the same length as the cells, with the longest reaching 59.67 μm. On DAY 23, nearly all neurites exceeded 80 μm in length, with the longest measuring 125.20 μm. The average number of neurites per neuron was important for assessing neuronal and local cortex functionality.[46]

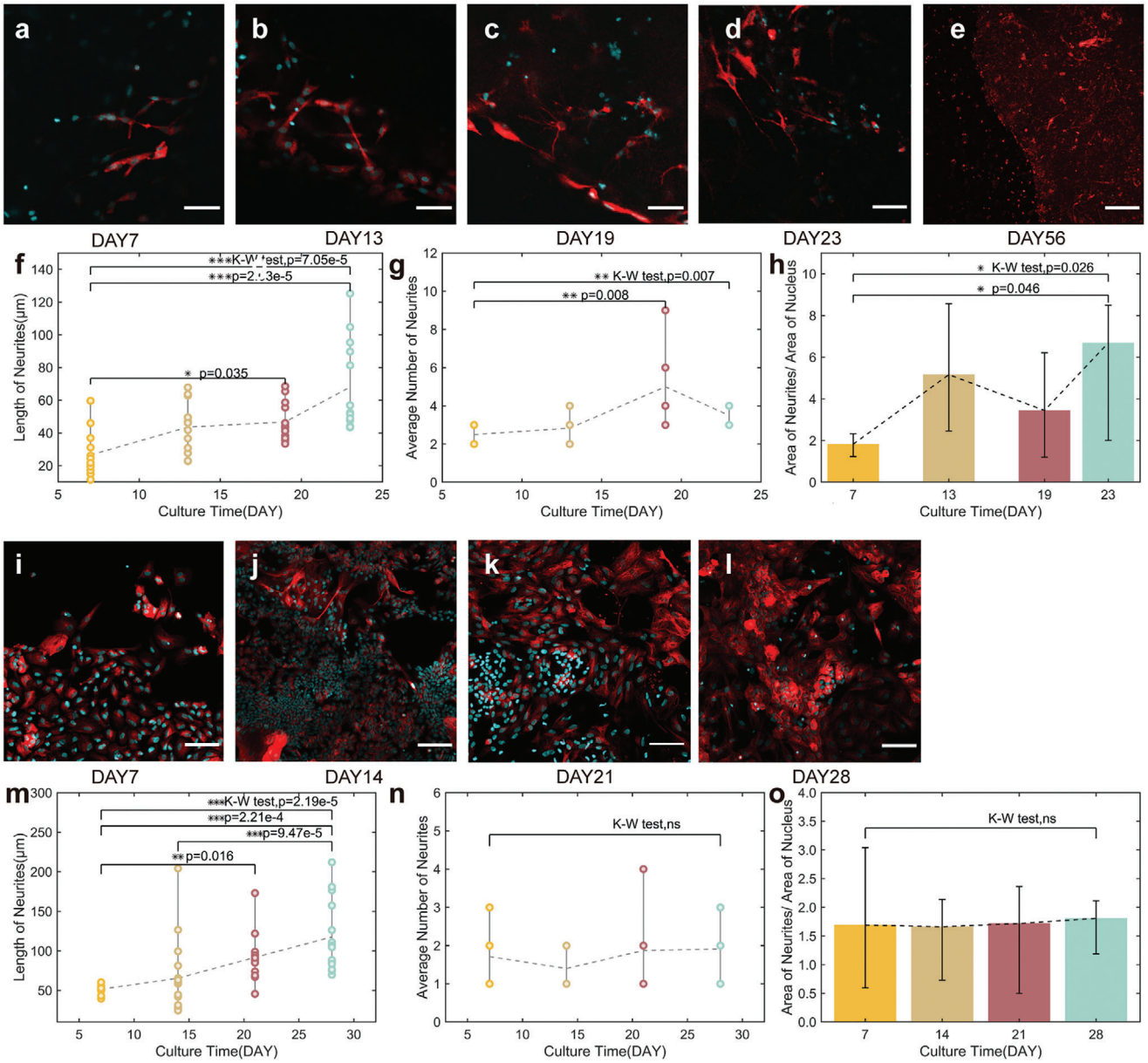

Figure 4. NPCs within constructs gradually formed neurites and were capable of integrating with living tissues. a–d) Immunofluorescence results of constructs on DAYS 7, 13, 19, and 23. Blue and red refer to DAPI and β-tubulin-iii, respectively. β-tubulin-iii was photographed in the thin area only because of noise from the materials. Scale bar, 50 μm. e) Immunofluorescence results of constructs cultured in vitro for over a month (DAY 56). The colors had the same meanings as in a-d. Scale bar, 200 μm. f) Statistical results of cell neurite lengths inside the constructs on culture DAYS 7, 13, 19, and 23. Each point referred to one neurite detected in view (n = 13). g) The average number of neurites per cell of the constructs on culture DAYS 7, 13, 19, and 23. Each point referred to one cell detected in view (n = 6). h) Area ratio of neurite to nucleus of the constructs on culture DAYS 7, 13, 19, and 23. (n = 6). i–l) Immunofluorescence results of 2D cultures on DAYS 7, 14, 21, and 28. Blue and red referred to DAPI and β-tubulin-iii, respectively. Scale bar, 100 μm. m-o) Analysis of neurite lengths (n = 9, 16, 9, 15), average numbers of neurites per cell (n = 7, 10, 8, 11), and area ratios of neurite to nucleus (n = 5) of 2D cultures. Data presented as mean with range. K-W tests were performed to clarify whether culturing time had a significant effect on neurite length, average number of neurites per cell, and area ratio of neurite to nucleus of 3D constructs and 2D cultures. The differences between groups of different dates were given through Dunn's multiple comparison tests. For all statistical images, *p < 0.05, **p < 0.01, and ***p < 0.001.

This study explored the average number of neurites to gauge the functional development of the constructs. A gradual increase followed by a noticeable decrease was observed over the one-month culture period (Figure 4g), possibly reflecting neurite growth and refinement within the constructs. However, the neurite count per neuron in the constructs was significantly lower than that of the natural human cortex (≈10^3), casting doubt on the representation of synaptic development in this construct. The developmental situation of the constructs was evaluated using the neurite-to-nucleus area ratio as a metric that combined neurite length and

count to indicate maturation degree. Despite certain fluctuations, this parameter showed that the constructs matured over the one-month culture period (Figure 4h). In contrast, although neurites grew over time in 2D cultures, the average number of neurites per neuron and the neurite-to-nucleus area ratio did not show a significant difference during the one-month culture. The absence of change in the neurites was possibly due to the high density of primary NPCs and the lack of a 3D environment. (Figure 4i–o)

Calcium signaling was a crucial function in evaluating neuronal activity. Constructs cultured for over a week were stained with Fluo-4 AM and sequential imaging was performed. As shown in **Figure 5**i, cells were identified and categorized as separate numbered regions of interest (ROI) using CellPose.[47] The percentage of active cells increased with culturing duration for 3D groups but not for 2D groups, which indicated that the 3D environment was beneficial for cell signal transmission. (Figure 5a). In addition, general higher intensity and shorter duration of signals from 3D constructs compared to those from 2D cultures also showed that cells were more active in 3D culture. (Figure 5b,c) The intensities of calcium signals increased in the first week but dropped from DAY 14, implying connection construction and stabilization. (Figure 5b) Additionally, the slight decrease in signal duration indicated the maturation of connections. Synchronous signals and intercellular calcium signal transmission originating from physically adjacent cells were observed in the constructs after two weeks of culturing. (Figure 5e–h; Videos S1 and S2, Supporting Information) The characteristics and patterns of these signals were consistent with previous studies on primary neural cells and iPSC-derived neural cells.[34,40] aCSF with high KCl and with glutamine and glycine (glu/gly) were applied to the constructs on DAY 7 to identify cell signaling in reaction to stimulation. Figure 5m showed that most cells responded to K+ while only some of them were sensitive to glu/gly, which corresponded with neural reactions reported in other work.[37] Calcium ions were employed in the system to crosslink alginate. In order to exclude the influence of foreign calcium ions, 2D NPC cultures with and without material dots were tested for calcium signals on DAYS 7, 14, and 21. (Figure S9, Supporting Information) The percentage of active cells, peak values, signal durations, and distributions showed the influence of calcium ions released as a result of the degradation of sodium alginate was relatively limited.

Electrical signals were recorded to investigate the communication between neurons and the maturity of neural development. The constructs were cultured for approximately five months to monitor the evolution of electrical functions. Electrical signals that were indicative of initial neural network formation were detected from the second week of culture. These signals demonstrated the acquisition of basic electrophysiological functions at an early stage. (**Figure 6**a) However, the percentage of active electrodes did not increase monotonically from week 2, possibly owing to the distribution of neurons settling after printing. The augmented numbers of spikes over time indicated the development of neural networks within the constructs. (Figure 6b) The amplitudes of the spikes did not change significantly before week 14 and stayed in the 0.033-0.522 mV range, which corresponded with normal local field potential (LFP) signals from natural neural tissues and organoids.[48,49] However, the amplitudes raised sharply on week 19 to an abnormal value compared to other research.[35] (Figure 6c) Differences were observed among groups in terms of average signal frequency. The trend of the mean value was an initial increase followed by a decrease over the culture period, while the maximum frequency increased with time (Figure 6d). The change in average signal frequency was potentially attributed to the combined effects of functional development in the early stages and limited external stimulation throughout the long-term culture period. In general, the electrical signal analysis revealed a developmental trajectory from newborn to normal and even pathological states. Initial network formation occurred in weeks 1–2. The establishment of normal connectivity occurred by week 14. The predominance of seizure-like activities (1.68±0.32 mV) occurred starting on week 14, which indicated the formation of aberrant connections among neurons. Adding the sodium channel blocker tetrodotoxin (TTX) to the constructs resulted in a significant reduction or disappearance of electrical signals, indicating a drug response similar to that of normal brain tissue (Figure 6e–h). The electrical signals remaining after TTX addition were considered noise and excluded from the analysis.

2.4. Constructs were Transplantable and Integrated into Hippocampi In Vivo

The in vitro results indicated that constructs had the potential for further development as implants for neural disorders, which was demonstrated by testing the implantability and integration of the constructs in vivo.

Grid constructs, with dimensions of 10 mm × 10 mm × 0.75 mm, were too invasive for the size of the rat brains. Consequently, dot constructs with a diameter of 1 mm and a height of 0.25 mm were designed and printed to minimize damage during implantation (Figure S1b and Code S2, Supporting Information). Dot constructs were printed and cultured for two weeks in vitro for live/dead staining and demonstrated no significant difference in viability between the grid and dot constructs (Figure S10 a-e,i,k, Supporting Information). Simulated transplantation processes were conducted on the dot constructs on DAY 5 to examine the impact on cell viability (Figure S10 f-h, j, Supporting Information). According to Figure S10k (Supporting Information), there was no significant difference in cell viability between the groups with and without the transplantation procedure. However, the mean values of cell viability from transplanted dots were slightly lower than those from original dots at the same time point. As illustrated in Figure S10k, j (Supporting Information), the dot constructs that underwent transplantation exhibited a reduction in size compared to their original counterparts but retained their 3D structure. In conclusion, the differences between grid and dot constructs were minimal, and the transplantation procedure influenced the sizes of constructs and viability of cells to an acceptable extent. Dot constructs with pure materials were transplanted into the hippocampus of P1 Wistar rats, and brain slices were obtained at 1, 3, 5, and 7 days post-transplantation. The areas of implanted constructs were identified through hematoxylin and eosin (HE) staining of brain slices. The staining results showed a complete degradation time of ≈10.29 to 33.83 days, which demonstrated the material could effectively protect the transplanted cells for approximately one month while gradually

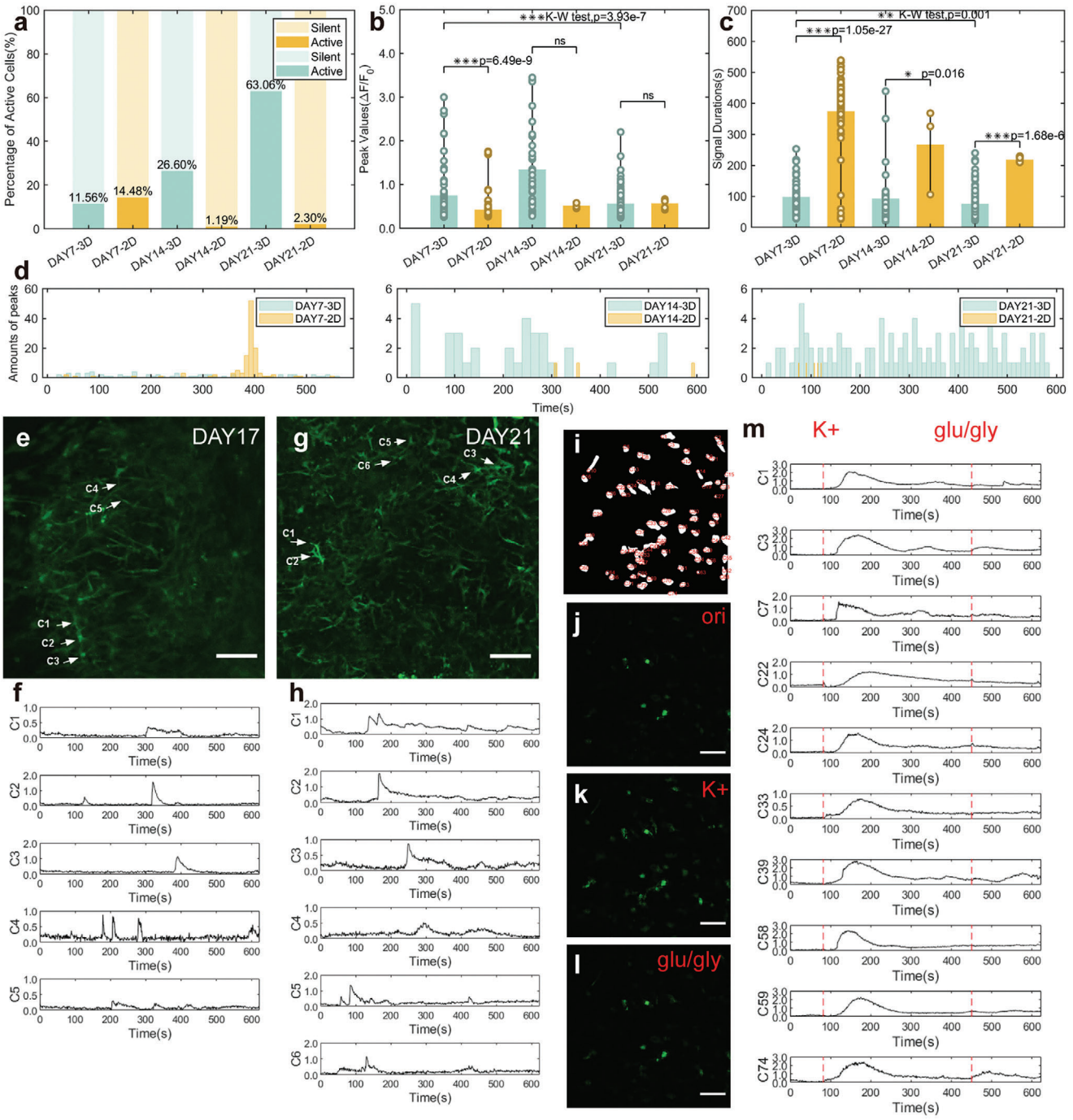

Figure 5. Calcium signals from cells within constructs demonstrated that basic function and signal connection were achieved in this model. a–d) Areas of cells were identified from original time sequence images by CellPose and artificially corrected. Calcium signals were collected and analyzed for active cell percentages, peak values, peak widths, and peak distributions. Five groups came from the 3D constructs on DAYS 7, 14, and 21 and 2D groups on DAYS 7, 14, and 21. (n = 519, 808, 94, 252, 111, 217) Nonparametric Kruskal-Wallis tests were performed on the 3D groups on DAYS 7, 14, and 21 to explore developmental influences, while Mann-Whitney tests were performed between corresponding 2D and 3D groups for differences. e–h) Synchronism and transmissions of signals detected and corresponding ROIs from constructs on DAYS 17 and 21. Neighboring cells formed a group. i–m) Stimulation tests on DAY 7 constructs. i represents cell areas identified and corresponding numbers. j–k) Images taken without treatment, after the addition of K+, cells after the addition of glu/gly, respectively. Scale bar, 100 μm. m) Responses from cells to external stimuli. The red lines show the time points of adding K+ and glu/gly, respectively.

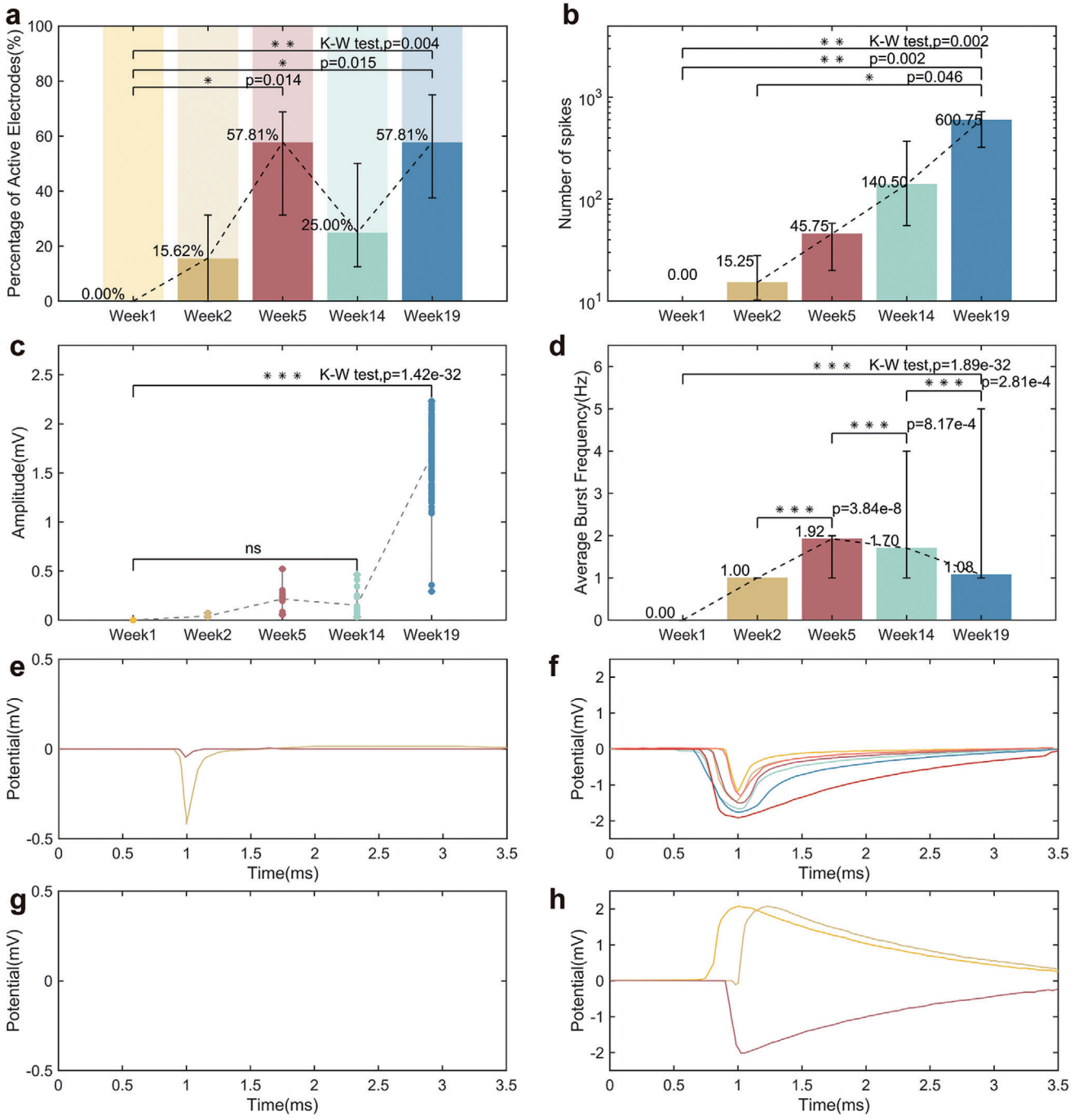

Figure 6. Electrophysiological tests demonstrated maturation and the spontaneous electrical activity of constructs increased throughout long-term culture. a) Percentages of active electrodes with signals on weeks 1, 2, 5, 14, and 19. ($n = 4$) b) Numbers of spikes identified and fitted by the MED64 system. ($n = 4$) c) Corresponding amplitudes of spikes. ($n = 61$, 188, 436, 2403) d) Corresponding average burst frequencies. Spikes within 1 s were considered a burst. Average burst frequency meant the frequency of spikes within a second. ($n = 61$, 188, 436, 2403) For all statistical analyses in this figure, nonparametric Kruskal-Wallis tests and multiple comparisons were performed to explore developmental influences. *$p < 0.05$, **$p < 0.01$, and ***$p < 0.001$. Data presented as mean with range. e–f) Spikes collected and classified by MED64 system (clear noises were excluded) from week 5 and 19. g–h) Signals remained from weeks 5 and 19 after treatment with TTX. The red signal in (f) was considered noise.

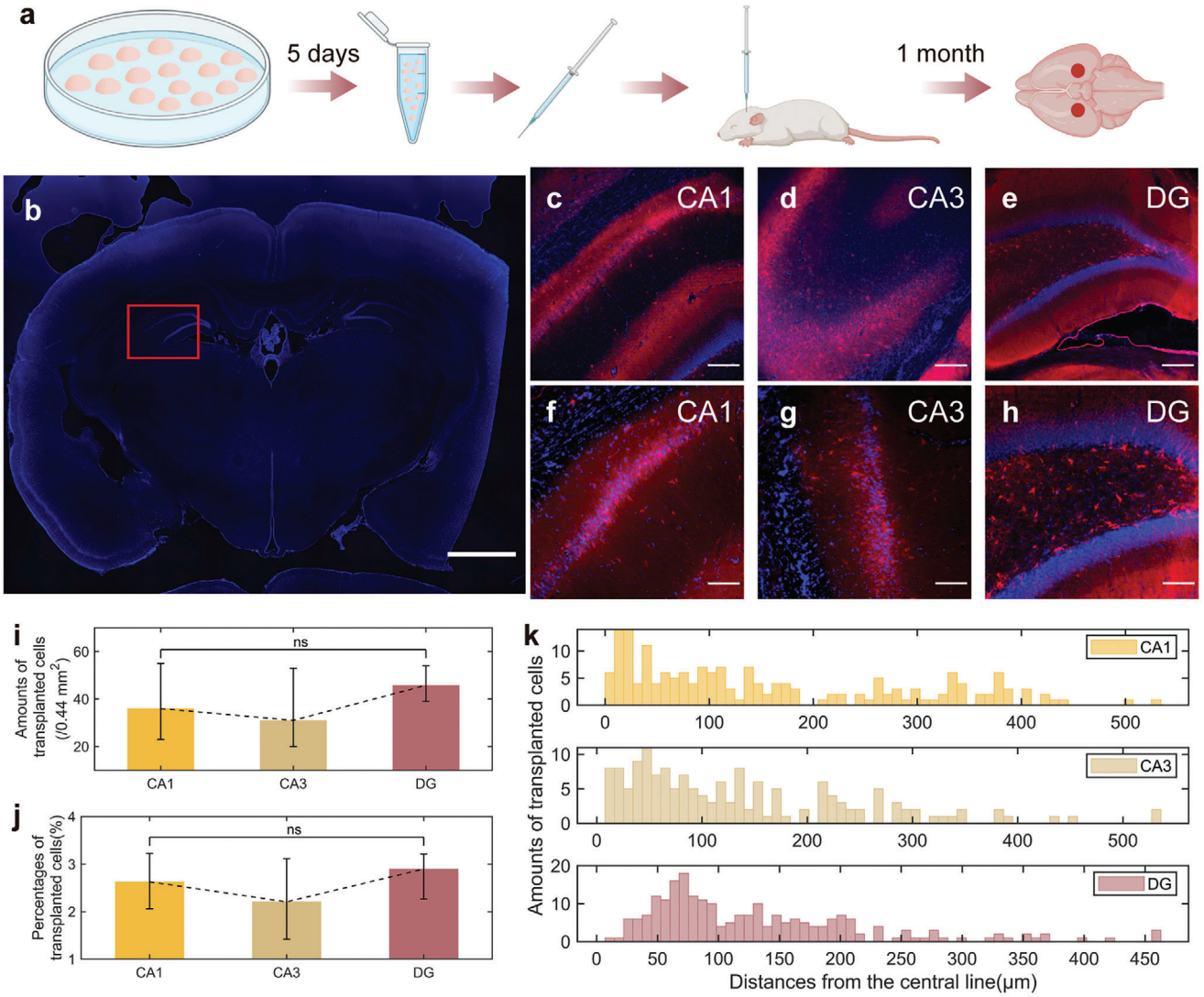

Figure 7. Implantation of developmental constructs into hippocampi of rats. a) Schematic of the implantation procedure for the new constructs. (Created with BioRender.com) b) Overall coronal brain slice of the rats. The red rectangle represented the hippocampal area of implantation. DAPI showed the nucleus. Scale bar, 2000 μm. c–e) Different areas of the hippocampus, CA1, CA3, and DG. Implanted NPCs were marked with mCherry, exhibiting red in images. DAPI showed the nucleus. Scale bar, 200 μm. f–h) Morphology features, especially the neurites of cells marked by mCherry (red). Scale bar, 100 μm. i) Amounts of implanted cells in an area of 0.44 mm^2 in the CA1, CA3, and DG regions. j) Proportion of implanted cells to total cells in the CA1, CA3, and DG regions, which referred to the xenogeneic ratio for this animal model. ANOVA tests showed no significant difference among groups in i and j. k) Distribution of implanted cells in hippocampi exhibited by distances from centers of cells to center lines (bright blue bands in DAPI channels) of the tissues.

degrading to provide spaces for both transplanted and host cells (Figure S11, Supporting Information).

Prior to implantation, the NPCs were labeled with mCherry via lentiviral infection for subsequent observation and printed into dot constructs. After a 5-day culture period, the constructs were implanted into the hippocampi of P1 Wistar rats using a syringe. The rats survived for over a month following the surgical implantation of cells without displaying any discernible behavioral abnormalities that might be attributed to the implantation process itself. After the one-month period, brain slices were obtained from the rats to identify the integration of the transplanted cells (**Figure** 7a). The intended implantation target was the CA1 region of the hippocampus (Figure 7b), but the actual incision was larger, encompassing areas beyond CA1. As depicted in Figure 7c–e, the implanted NPCs were found in both the CA1 area and the neighboring CA3 and DG regions but not in other regions of the brain. The migration within the hippocampus offered insight into neural cell behavior during development and recovery. Although cell counts and percentages were highest in the DG region (45.8 ± 5.9) per 0.4 mm^2 and (2.90 ± 0.41) %, followed by the CA1 and CA3 regions, no significant differences ($p = 0.17$ and $p = 0.21$, respectively) were observed among these areas (Figure 7i,j), which suggested that the transplanted cells dispersed evenly throughout the entire

hippocampus. Further analysis of the integration between cells in constructs and in vivo could enhance the development of stem cell therapy for brain tissue recovery, providing guidance for the optimal implantation location and quantity of NPCs used. Regarding distribution, implanted cells in the CA1 and CA3 regions were arranged in compact patterns near the central lines of the tissues, whereas cells in the DG region were more loosely distributed along the gyrus, away from the center (Figure 7k). In more detailed observations, distinctly marked cells with neurites were identified. Cells near the central line resembled pyramidal neurons in morphology, with long neurites, whereas cells farther from the center displayed less of these properties. Compared to the in vitro culture results, the cell arrangements were more akin to the layered structure and orientation of the natural cerebral cortex, with a higher cell density observed (Figure 7f–h).

3. Discussion

3.1. Defined Biomimetic Mechanical Environments Benefited Neurite Growth and Long-Term Culture

The main principle in designing the material system was to mimic the mechanical properties of human brain tissue. The brain is inherently inhomogeneous, nonlinear, and viscoelastic, with mechanical properties that vary by region, species, age, and health condition.[50,51] The compressive elastic modulus is ≈2.6 kPa for neonatal mice and ≈5.7 kPa for adult mice.[52] Human brain tissue exhibits an elastic modulus from a few hundred Pascals to several kilo Pascals.[51,54,55] In addition, the stiffness of brain tissue increases as embryos develop.[56] Therefore, the material system was engineered with an initial modulus of ≈7 kPa, slightly above the typical brain tissue range but within the bounds of health. The system then experienced a minor increase in stiffness (from ≈6 kPa to 12 kPa) post-crosslinking. The storage modulus was considerably lower, in the range of hundreds of Pascals, aligning with human brain properties.[57] Despite the addition of aprotinin to prevent material hydrolyzation, long-term hardening was not observed, likely due to the high starting elastic modulus. Material stiffness is known to influence cell differentiation and neurite outgrowth. Softer materials, with elastic moduli on the order of kPa, were demonstrated to be beneficial for brain-direction differentiation,[58] while matrices with stiffness between 1000 and 10 000 Pa are more conducive to glial cell generation.[59] The designed constructs, with their final modulus, were capable of supporting brain genesis, yet they tended to favor glial differentiation over neuronal differentiation. Nevertheless, over 90% differentiation into neural direction and neuron-glia sequences were detected, which suggested that the developed culture environment is conducive to brain-like differentiation. Previous studies have explored printing NSCs within hydrogels of low elasticity.[39,41] This study proposed a material system with a relatively high elastic modulus and excellent formability, which was well-suited for the fabrication of implants with heights in the z-direction. Gelatin and alginate contributed to NPC proliferation and stemness in the initial week of culturing, while fibrinogen was conducive to adapting to the different needs of mechanical properties from neural progenitor cell proliferation, differentiation, maturation, and aging. The combination of the material system, stemness-maintenance medium, and self-differentiation medium successfully directed NPC proliferation and differentiation, maintaining cell-material interactions for over 19 weeks with the support of aprotinin. The culturing duration was critical, as longer-term cultures allowed constructs to achieve a more mature state under controlled conditions. Furthermore, the system allowed for the precise addition of components to investigate their contribution to brain tissue. This capability allowed for the adjustment of constructs according to different design requirements and the investigation of unit functions within brain tissue.

3.2. The Differentiation and Functionalization of Tissue Constructs Recapitulated Key Aspects of Early Central Nervous System Development

The generation of cells in the early human central nervous system adheres to conserved spatiotemporal patterns: neuroepithelial stem cells (NECs) proliferate in the ventricular zone (VZ), evolve into radial glial cells, give rise to excitatory and inhibitory neurons, and finally generate glial cells. This process involves neural progenitors migrating to their target areas to establish layers and regions.[44] In this studiy, hiPSC-derived NPCs followed a similar sequence of proliferation and differentiation, initially producing neurons and subsequently generating glial cells. However, the proportion of neurons in the designed constructs was between 80% and 90%, surpassing the range of 60% to 80% typically observed in mouse models, highlighting differences between the designed constructs and natural conditions. The constructs also mirrored key milestones in human brain development. Neuron production surged within a week after separation from the stemness-maintenance culture medium, paralleling the human brain development timeline from approximately six post-conception weeks (pcw) to 20 pcw. Neuritogenesis commenced in the first week, and rudimentary networks formed by the second week, aligning with human development at ≈14 pcw. Gliogenesis began after a week of culture and continued, resembling the human timeline from ≈12 pcw into adolescence. The development of electrophysiological functions in the models from week 2 to week 19 corresponded with synaptogenesis and neuronal maturation in humans from ≈15 pcw through adolescence. Synapse refinement was also partially replicated in the model after one month of culture, a process in humans that starts around birth and continues to adulthood. These developments demonstrated the ability of the construct to serve both as a platform for implants at different developmental stages and as a tool for investigating the development of the early human brain. Currently, the function region of human brain has been investigated systematically, while the formation of functional units within is still elusive. The constructs possess the potential to build brain constructs with certain amounts of NPCs in required positions to mimic early development of representative function regions through cell differentiation, thereby facilitating the investigation of how specific functional units of the brain develop over time. In summary, the construct successfully replicated the developmental process and certain features of early human brain development, both pre- and post-birth. Nevertheless, further investigation is required to examine the mechanisms underlying cell migration and the formation of morphological characteristics in this model.

3.3. Implantation and Neural Drug Reaction Proved the Model to be Competitive for drug Testing, Stem Cell Treatment, and Further Epileptic Brain Disease Models

The material system demonstrated excellent formability while maintaining physiological cell functions, enabling the creation of diverse constructs with specifically designed structures and defined multicellular distributions. These capabilities aligned with the requirements of personalized medicine, where mechanical strength was crucial for 3D geometry retention—a challenge often unmet by liquid injection stem cell therapies.[60] Additionally, NPCs from another hiPS cell line from human peripheral blood mononuclear cells (hPBMCs) could also survive and function in constructs, thereby expanding the resources of upstream cells in clinical transplantation (Figure S8, Supporting Information). The application of pre-differentiated NPCs reduced the risk of tumor formation and ensured their potential to differentiate into the required cell types within the hippocampus. Implantation results confirmed that the constructs could distribute NPCs uniformly across different hippocampal regions and maintained cell presence in the targeted area for over a month without inducing any apparent symptoms of infection or immune rejection. Morphological analysis of the implanted cells revealed neurite formation and aligned distribution, validating the efficacy of the constructs as viable in vivo implants for stem cell therapy. However, numerous tasks remained before the implementation of this 3D-printed construct in clinical trials. First, as an invasive treatment, construct implantation was riskier than traditional liquid injection. Therefore, the surgical design for clinical trials requires further optimization. The brains of rats were relatively small in comparison to that of humans, and implants with a comparable size to the grid constructs would result in significant traumatic injury. Given that the human brain is ≈1000 times larger than the rat brain,[61,62] with a size ratio of at least 10, the grid construct developed in this study for transplantation in the human brain was comparable to the dot construct for transplantation in the rat brain. Despite the similarity, size had an influence on the resolution of printing and interactions of constructs with host tissues. Therefore, it is necessary to transplant constructs with larger sizes into large animal models in order to gain further insight. Second, it is necessary to fully explore the integration with local neural circuits and functional recovery through calcium imaging in vivo and transplantation into diseased or injured animal models.

A distinctive feature of the construct was its developmental electrophysiological function, showing neuronal maturation and the responsiveness of the construct to external stimuli in real-time. The immediate influence observed following the TTX application underscored the ability of the model for drug testing, demonstrating that small-molecule medications such as TTX could permeate the hydrogel and impact the neural cells within. Therefore, this model is well suited for investigating various pharmaceutical and environmental factors influencing the early cerebral cortex. The unusually high spike amplitudes (≈2 mV, in contrast to the hundreds of microvolts typical for standard electrical signals) and burst occurrences within a brief timeframe during week 19, as illustrated in Figure 6c, resembled seizure-like signals. Although this abnormal discharge pattern was not consistently observed across samples, and spontaneous epileptic symptoms in the models were not definitively established, the occurrence of such phenomena indicated the potential of this construct to serve as an epilepsy model. This could be achieved either by using iPSCs from epilepsy patients as the seed cells or through pharmacological interventions to normal models.

4. Conclusion

In conclusion, a precisely engineered brain-like construct was developed utilizing a biomimetic material system and 3D-printed NPCs.

The NPCs in this construct differentiated under optimal conditions and exhibited the functional characteristics of neural cells, including calcium and electrical signaling, for up to 19 weeks, which surpassed the longevity of the current printed constructs of around one month.[38,39,41] This model effectively mimicked human brain development, encompassing essential processes such as the sequential differentiation of NSCs, neurogenesis, gliogenesis, the establishment of neural networks, and the maturation of neural functions before and after birth. Furthermore, the occurrence of seizure-like signals in long-term cultures suggested that this model might be useful in constructing epilepsy models and studying other neurological conditions.

Compared to existing stem cell therapy implants, this model offers higher controllability, reproducibility, and precision in both the temporal and spatial dimensions. The material system ensured excellent formability while preserving cellular physiological functions, enabling the construction of implants with customized structures and multicellular distributions. According to our knowledge, this is the first work to test the feasibility of 3D-printed brain implants in vivo. The constructs can maintain designed shapes for at least one week after transplantation. The mechanical strength of the implants enabled the secure fixation of implanted cells during surgical procedures and ensured their retention in the rat hippocampus in vivo for over one month. In vivo results further highlighted the significance of this model for advancing stem cell therapeutic applications.

Nevertheless, current in vivo testing was constrained by the limited culture duration, lack of models with neural disorders, and limitation of applied species. Furthermore, the therapeutic efficacy of these constructs for neural disorders such as Alzheimer's, epilepsy, and stroke remains to be validated. Future research will focus on enhancing the functional integration of the constructs into host neural networks, assessing their long-term survival, and evaluating their effects on cognitive repair. Interdisciplinary collaboration and partnerships with clinical institutions are essential to realize the potential of this brain repair treatment, broaden its application to a spectrum of neurological conditions, and progress the technology toward clinical readiness.

5. Experimental Section

Generation and Culture of Neural Progenitor Cells: Human induced pluripotent stem cells (ATCC ACS-1019) were cultured in mTeSR Plus medium (STEMCELL Technologies, USA) until they were ready for passaging. Cells were dissociated using Gentle Cell Dissociation Reagent (STEMCELL Technologies, USA) to separate them from the culture plate and disaggregate them into single cells. These single iPSCs were then suspended in STEMdiff Neural Induction Medium (STEMCELL Technologies,

USA) with 10 µM Y-27632 (STEMCELL Technologies, USA) and seeded onto plates coated with Corning Matrigel. The medium was fully replaced daily with STEMdiff Neural Induction Medium until the cultures were prepared for passaging. Cells were dissociated and passaged twice using ACCUTASE (STEMCELL Technologies, USA) before the NPCs were finalized. Another human induced pluripotent stem cell line (IxCell, China) from human peripheral blood mononuclear cells (hPBMCs) were purchased and underwent the same culture and induction procedure to obtain NPCs for subsequential experiments to prove the reproducibility of this work. These NPCs were maintained in a 5% CO_2 incubator at 37 °C with a daily medium change of STEMdiff Neural Progenitor Medium (STEMCELL Technologies, USA) and were ready for construct assembly by Passage 6. For 2D control experiments, the STEMdiff Forebrain Neuron Differentiation Kit and STEMdiff Forebrain Neuron Maturation Kit (STEMCELL Technologies, USA) were applied according to the product guidelines. NPCs were cultured for over four weeks before being utilized in control groups.

Bioink Components Preparation and Mixing Methods: The bioink was formulated with gelatin, sodium alginate, and fibrinogen to achieve a biomimetic elastic modulus, appropriate biocompatibility, and long-term stability. A 20% (w/v) stock solution of gelatin (Sigma, USA) was prepared in 0.9% (w/v) sodium chloride and pasteurized, then stored at 4 °C. Sodium alginate (Sigma, USA) was similarly prepared as a 1% (w/v) stock solution, pasteurized, and stored at 4 °C. 40 $mg{\cdot}mL^{-1}$ fibrinogen (YUANYE, China) was dissolved in 0.9% (w/v) sodium chloride and stored at −20 °C. The bioink comprises 200 µL of 20% (w/v) gelatin, 100 µl of 1%(w/v) SA, 200 µl of 40 $mg{\cdot}mL^{-1}$ fibrinogen, and 200 µL of cell suspension containing more than 2.5×10^6 cells. The materials were combined in the following sequence to prepare the bioink: sodium alginate, fibrinogen, cell suspension, and gelatin. This process was carried out to ensure a smooth homogeneous mixture suitable for use as bioink.

3D Printing of In Vitro Cell Constructs and Subsequent Culture Procedures: A layer-by-layer grid construct was designed to accommodate the lamellar structure of the brain and the nutritional needs of the cells for in vitro culture. Two structure sizes were created: 10 mm × 10 mm × 0.75 mm, and 7 mm × 7 mm × 0.75 mm, with a line spacing of 1.2 mm and a single-layer height of 0.25 mm. The larger size was used for culture and functional verification experiments, while the smaller was used for electrophysiological performance tests. The dimensions were selected based on dish size and the necessity for cells within the structure to access nutrients and oxygen efficiently. A dot construct was designed for in vivo implantation research with a size of Φ1 mm × 0.25 mm.

The bioprinter (BIOMAKER 4; SUNP BIOTECH, China) was sterilized with UV light for 20 min to ensure a sterile internal environment. Printing parameters were optimized for the best outcomes, setting nozzle and bed temperatures to 15 °C and 10 °C, respectively, according to the rheological property of the bioink. The inner diameter of the nozzle was chosen as 0.51 mm to minimize shear forces on the cells, and the printing and extrusion speeds were set to 5 $mm{\cdot}s^{-1}$ and 1.1 $mm^3{\cdot}s^{-1}$, respectively.

The bioink mixture was prepared and loaded into a 1 mL syringe, which was then precooled at 4 °C for 4 min prior to printing. Once the syringe was mounted on the printer, the printing process was performed automatically using predetermined parameters. Immediately after printing, the structure was transferred to a hood for chemical crosslinking with 2% $CaCl_2$ for 3 min at room temperature. Subsequently, the medium containing 10 $U{\cdot}mL^{-1}$ thrombin (YUANYE, China), 0.36 $U{\cdot}mL^{-1}$ glutamine transaminase (YUANYE, China), and an appropriate concentration of penicillin-streptomycin solution (Beyotime, China) was added to further crosslink the gelatin and fibrinogen for 2 to 4 h at 37 °C. For ongoing culture, STEMdiff Neural Progenitor Medium supplemented with 20 $\mu g{\cdot}mL^{-1}$ aprotinin and penicillin-streptomycin solution was used for maintaining stemness, while Neurobasal Medium (Gibco, USA) with the same supplements was used for long-term culture and self-differentiation.

Characterizations of Materials: The elastic modulus of the crosslinked bioinks was tested using a Bose ElectroForce 3200 compression system (Bose Corp., USA). The 6 mm diameter and 4 mm high samples were shaped using nylon molds and crosslinked in situ. The samples were cultured for 1, 4, 7, 10, and 14 DAYS and then analyzed for compressive elastic modulus in 0.9% (w/v) NaCl. During testing, the samples were compressed to 75% of their original height at a rate of 1 $mm{\cdot}min^{-1}$, with force and displacement recorded. Stress-strain data from these tests were linearly fitted between strains of 0 and 0.1 to calculate the elastic modulus.

The rheological properties of the bioink were measured using a rheometer (MCR301, Anton Paar, Austria) with a 25 mm diameter cone plate, identifying the optimal printing temperature. The analysis was performed while varying the temperature from 37 °C down to 4 °C, using 1% strain and a sample frequency of 1 Hz. The loss and storage moduli were calculated, and the temperature at which these two moduli intersected was deemed optimal for printing.

Fourier transform infrared (FTIR) analysis was conducted to assess the stability of the bioink components on DAYS 1, 4, 7,10, and 14, using pure gelatin and sodium alginate as controls. The samples were rapidly cooled in liquid nitrogen and freeze-dried by lyophilizer (LGJ-12, SONGYUANHUAXING Technology, China). They were then analyzed using an FTIR spectrometer (IRTracer-100, SHIMADZU, Japan) in the Chemical Engineering Department of Tsinghua University.

The shape fidelity and degradation tests were conducted on materials in the same shape with cell-loaded constructs. Printing and crosslinking procedures were also consistent. Samples were cultured in aCSF with penicillin and streptomycin to mimic the environment following transplantation into the hippocampi. Samples were collected at designated time points to measure sizes and weights with a stereo microscope (SMZ800N, Nikon, Japan) and electronic balance (PX124ZH, OHAUS, China).

Assessment of Cells: To verify cell viability within the constructs, Calcium AM and PI (DOJINDO, Japan) were dissolved in DPBS (Sigma, USA) and applied to the structures at concentrations of 2 µM and 4.5 µM, respectively. After two washes, the dyes were added to the culture dishes, and the staining lasted for 20 min, followed by three washes to remove any residual dye. Laser scanning confocal microscopy (TI-FL, Nikon, Japan, and FV3000, Olympus, Japan) with 515 nm and 580 nm lasers was used to image live (green) and dead (red) cells. Z-stack images were acquired as per the system recommendations, and 3D views were provided by the system's software. Cell counting was conducted using randomly selected images and the Cell Counter tool using Fiji open-source software.

For immunocytochemistry (ICC), Anti-Nestin (STEMCELL Technologies, USA), anti-NeuN (Millipore, USA), and anti-β-tubulin (eBioscience, USA) antibodies were used to distinguish different cell types. Samples were collected on DAYS 7 and 14, rinsed twice with DPBS, and fixed in 4% paraformaldehyde for 30 min. After three washes, samples were permeabilized with 0.1% Triton-X-100 and 0.1% BSA in DPBS for 30 min. A blocking buffer of 2% BSA in DPBS was used for 1 h. The samples were then incubated with primary antibodies diluted in 0.1% BSA in DPBS, which also contained DAPI (Invitrogen, USA), overnight at 4 °C. For antibodies requiring secondary antibodies, the samples, after three washes, were further incubated with the appropriate secondary antibodies and DAPI in 0.1% BSA in DPBS for 1 h in the dark. After three final washes, the samples were ready for imaging. Laser scanning confocal microscopy (TI-FL, Nikon, Japan, and FV3000, Olympus, Japan) utilized lasers at 590, 555, 515, 488, 420, and 405 nm for excitation of the fluorescent markers.

For flow cytometry, anti-Nestin (STEMCELL Technologies, USA), anti-NeuN (Millipore, USA), and anti-GFAP (eBioscience, USA) antibodies were used to analyze cell differentiation. On the harvest DAY, the constructs were washed thrice with HBSS (ThermoFisher, USA) and treated with 1 $mg{\cdot}mL^{-1}$ collagenase I (Beyotime, China) for 8–9 h at 37 °C. The cells were then filtered through a 40 µm sieve and centrifuged at 300 x g for 3 min. The cell pellet was resuspended in staining buffer (1% BSA in DPBS with ProClean, Beyotime, China) to a concentration of 2×10^4 to 1×10^6 cells per tube. The cells were fixed with 4% paraformaldehyde at room temperature for 30 min, centrifuged at 500 x g for 5 min to remove the supernatant, and washed twice with permeabilization buffer (0.1% Triton-X-100, 2% BSA, 2 mM EDTA, and ProClean in DPBS). The antibodies, diluted in staining buffer, were added to the cells, which were then incubated in the dark for 1 h. After a wash with permeabilization and stain buffers, the cells were resuspended in staining buffer for flowcytometry analysis using a FACSAria II (BD, USA), with data processed in FlowJo software.

Calcium assays using Fluo 4-AM (DOJINDO, Japan), were conducted to assess live cell activity or neural functions within the constructs. The

constructs were washed three times with HBSS and then incubated with 5 μM Fluo 4-AM for 60 min at 37 °C. Following another three HBSS washes, the constructs were maintained in HBSS for 30 min at 37 °C. Observations were made using a laser confocal microscope (FV3000, Olympus, Japan) with 488 nm laser excitation. Each recording lasted for 10 mins. For stimulation testing, aCSF with high KCl (55.4 mM) and with glutamate (100 μM) and glycine (100 μM) were prepared according to the formulation provided in the reference.[37] Samples were given stimulation for 10 s per time with intervals of at least 200 s Cell recognition was facilitated by CellPose,[47] and signal analysis was conducted using MATLAB. In order to exclude the influence of foreign calcium ions, 2D NPC cultures with and without material dots were tested for calcium signals on DAYS 7, 14, and 21.

Electrophysiological tests are essential for understanding the functionalities and connections among cells within the constructs. Neural communication was studied through electrical signals captured by contact electrodes. A 64-channel multiple electrode array (MEA) system was used to collect electrical signals from cells in the vicinity, with the MED64 recording system (Japan) both recording from and stimulating the cells via the electrodes. The MEAs were thoroughly washed three times, first with distilled water, then 75% alcohol, and again with distilled water, followed by 15-min of UV light sterilization. Post-sterilization, the electrodes were covered with 0.005% polyethyleneimine (PEI) in a 25 mM borate buffer (pH 8.4) and left at room temperature for 1 h. After removing the PEI solution and washing with distilled water, the MEAs were dried in a clean environment overnight. Matrigel coating was used to the MEAs for 1 h at room temperature to ensure optimal cell-probe adherence. Following the removal of Matrigel, constructs were promptly printed onto the MEAs. During various culture periods, the electrodes were connected to the MED64 system, maintained at 37 °C, and signal recording was carried out for at least 1 h. To evaluate the influence of drugs, 0.5 μM TTX (MREDA, China) was introduced into the culture medium, with signal recording extended for another 1 h. For stimulation experiments, pulse signals of 2 μA at frequencies of 1, 2, and 4 Hz were used through channel 28 for 5 s at 5 min intervals (one trace).

Implantation of Constructs: NPCs were marked with an mCherry-labeled lentivirus for easy identification. To test the potential for in vivo culturing and implantation, the structures were fabricated as hemispherical shapes with diameters under 1 mm, employing the same printing, crosslinking, and culture protocols as standard in vitro practices. P1 Wistar rats were purchased from Vital River Laboratory (Animal Technology, Beijing, China) and maintained under standard conditions at the Tsinghua University Animal Facility (license number: SYXK 2019-0016) and Beihang University (license number: SYXK 2023-0036). Rats were anesthetized with 0.2% sodium pentobarbital (5 mL·kg^{-1}) and positioned in a stereotaxic apparatus (G1297201-001, RWD, China) before operation. Approvals were given by Beijing Municipal Science & Technology Commission, Administrative Commission of Zhongguancun Science Park. Target areas were shaved, and skins were cut. H_2O_2 was applied to remove surface tissue. Constructs on DAY 5 were collected from the culture dish and made into suspension with culture medium. The suspension was loaded in a 1 mL syringe with a 26G needle and constructs were implanted into the hippocampi of P1 Wistar rats via an injection pump with a volume of 200 μL per time. The rats were then monitored for 10 min to ensure the absorption of any fluids before being sutured closed. They were then housed under a 12 h:12 h light-dark cycle (lights on at 8:00) with food and water provided. For integration assessment, the rats were cultured for a month, euthanized, and sectioned for brain slices. DAPI staining was employed to identify all the cells. For biodegradation assessment, brain slices were obtained after 1, 3, 5, and 7 DAYS of culturing. Hematoxylin and eosin (H&E) staining were applied to identify the implanted constructs and host tissues.

Statistical Analysis: In the text, data are presented as mean values with their corresponding standard deviations (± SD). For all data analyzed for significant differences, the sizes are n≥3. The normality of the data underwent Shapiro-Wilk testing, and a $p > 0.05$ indicated that the original data conformed to a normal distribution. If the data did not pass the normality test, nonparametric Mann-Whitney, Kruskal-Wallis, and Dunn's multiple comparison tests were applied, otherwise, ANOVA and t-tests were conducted. For two-group comparison, a t-test was conducted to identify the differences. For three or more groups, statistical analysis was conducted using one-way analysis of variance (ANOVA) after the Levene test for equal variance, while data with unequal variance underwent Welch's ANOVA tests. If significant differences were found ($p < 0.05$), post hoc tests were conducted, and p values were corrected through Tukey's honestly significant difference (HSD) multiple comparisons test or Dunnett's T3 multiple comparisons test. GraphPad Prism and MATLAB were used for all statistical analyses. $p < 0.05$ was considered statistically significant. Significance levels were denoted by $*p < 0.05$, $**p < 0.01$, and $***p < 0.001$.

Supporting Information

Supporting Information is available from the Wiley Online Library or from the author.

Acknowledgements

The authors acknowledge Yue Sun and Jingjing Wang of the Center of Biomedical Analysis, for their assistance with the laser confocal microscopy (Olympus, FV3000, Japan). This work was funded by the National Natural Science Foundation of China. **Funding**: The National Nature Science Foundation of China No.: 31 700 928 (SY).

Conflict of Interest

The authors declare no conflict of interest.

Author Contributions

All authors commented on and/or edited the manuscript. K.G. performed background research. K.G., Y.S., X.L., S.W., A.S. performed writing. K.G., Y.S., M.Y., W.C., C.H., C.L., C.X., H.Z. performed experiments and analysis. Y.S., F.L., K.G., W.S. performed experimental design.

Data Availability Statement

The data that support the findings of this study are available in the supplementary material of this article.

Keywords

bioprinting, brain-like constructs, neural development, neural progenitor cells, stem cell therapy

Received: April 18, 2024
Revised: August 27, 2024
Published online: September 10, 2024

[1] J. Rodríguez-Pallares, M. García-Garrote, J. Parga, J. Labandeira-García, *Neural Regen Res* **2023**, *18*, 478.
[2] A. Genchi, E. Brambilla, F. Sangalli, M. Radaelli, M. Bacigaluppi, R. Furlan, A. Andolfo, D. Drago, C. Magagnotti, G. M. Scotti, R. Greco, P. Vezzulli, L. Ottoboni, M. Bonopane, D. Capilupo, F. Ruffini, D. Belotti, B. Cabiati, S. Cesana, G. Matera, L. Leocani, V. Martinelli, L. Moiola, L. Vago, P. Panina-Bordignon, A. Falini, F. Ciceri, A. Uglietti, M. P. Sormani, G. Comi, et al., *Nat. Med.* **2023**, *29*, 75.

[3] S. Srivastava, R. Ahmad, S. K. Khare, *Eur. J. Med. Chem.* **2021**, *216*, 113320.
[4] D. Kuriakose, Z. Xiao, *IJMS* **2020**, *21*, 7609.
[5] Md. Rahman, Md. Islam, M. Islam, Md. Harun-Or-Rashid, M. Islam, S. Abdullah, M. Uddin, S. Das, Md. Rahaman, M. Ahmed, F. Alhumaydhi, T. Emran, A. Mohamed, M. Faruque, M. Khandaker, G. Mostafa-Hedeab, *Biology* **2022**, *11*, 147.
[6] Z.-H. Zhu, F. Jia, W. Ahmed, G.-L. Zhang, H. Wang, C.-Q. Lin, W.-H. Chen, L.-K. Chen, *Neural Regen Res* **2023**, *18*, 404.
[7] G.-L. Zhang, Z.-H. Zhu, Y.-Z. Wang, *WJSC* **2019**, *11*, 817.
[8] Y. Jin, E. Mikhailova, M. Lei, S. A. Cowley, T. Sun, X. Yang, Y. Zhang, K. Liu, D. Catarino da Silva, L. Campos Soares, S. Bandiera, F. G. Szele, Z. Molnár, L. Zhou, H. Bayley, *Nat. Commun.* **2023**, *14*, 5986.
[9] M. Alessandrini, O. Preynat-Seauve, K. De Briun, M. S. Pepper, *S. Afr. Med. J.* **2019**, *109*, 70.
[10] R. Sakthiswary, A. A. Raymond, *Neural Regener. Res.* **2012**, *7*, 1822.
[11] J. Mertens, M. C. Marchetto, C. Bardy, F. H. Gage, *Nat. Rev. Neurosci.* **2016**, *17*, 424.
[12] Y. Zhang, C. Pak, Y. Han, H. Ahlenius, Z. Zhang, S. Chanda, S. Marro, C. Patzke, C. Acuna, J. Covy, *Neuron* **2013**, *78*, 785.
[13] C. Wang, M. E. Ward, R. Chen, K. Liu, T. E. Tracy, X. Chen, M. Xie, P. D. Sohn, C. Ludwig, A. Meyer-Franke, *Stem Cell Rep.* **2017**, *9*, 1221.
[14] S. P. Paşca, *Nature* **2018**, *553*, 437.
[15] M. A. Lancaster, M. Renner, C.-A. Martin, D. Wenzel, L. S. Bicknell, M. E. Hurles, T. Homfray, J. M. Penninger, A. P. Jackson, J. A. Knoblich, *Nature* **2013**, *501*, 373.
[16] K. W. Kelley, S. P. Paşca, *Cell* **2022**, *185*, 42.
[17] O. Revah, F. Gore, K. W. Kelley, J. Andersen, N. Sakai, X. Chen, M.-Y. Li, F. Birey, X. Yang, N. L. Saw, S. W. Baker, N. D. Amin, S. Kulkarni, R. Mudipalli, B. Cui, S. Nishino, G. A. Grant, J. K. Knowles, M. Shamloo, J. R. Huguenard, K. Deisseroth, S. P. Paşca, *Nature* **2022**, *610*, 319.
[18] D. Jgamadze, J. T. Lim, Z. Zhang, P. M. Harary, J. Germi, K. Mensah-Brown, C. D. Adam, E. Mirzakhalili, S. Singh, J. B. Gu, R. Blue, M. Dedhia, M. Fu, F. Jacob, X. Qian, K. Gagnon, M. Sergison, O. Fruchet, I. Rahaman, H. Wang, F. Xu, R. Xiao, D. Contreras, J. A. Wolf, H. Song, G.-L. Ming, H.-C. I. Chen, *Cell Stem Cell* **2023**, *30*, 137.
[19] Y. Shi, L. Sun, M. Wang, J. Liu, S. Zhong, R. Li, P. Li, L. Guo, A. Fang, R. Chen, W.-P. Ge, Q. Wu, X. Wang, *PLoS Biol.* **2020**, *18*, e3000705.
[20] E. Garreta, R. D. Kamm, S. M. Chuva De Sousa Lopes, M. A. Lancaster, R. Weiss, X. Trepat, I. Hyun, N. Montserrat, *Nat. Mater.* **2021**, *20*, 145.
[21] S. Aqel, N. Al-Thani, M. Z. Haider, S. Abdelhady, A. A. Al Thani, F. Kobeissy, A. A. Shaito, *Biology* **2023**, *13*, 21.
[22] Y. Wang, E. R. Zoneff, J. W. Thomas, N. Hong, L. L. Tan, D. J. McGillivray, A. W. Perriman, K. C. L. Law, L. H. Thompson, N. Moriarty, C. L. Parish, R. J. Williams, C. J. Jackson, D. R. Nisbet, *Nat. Commun.* **2023**, *14*, 457.
[23] J. Li, D. Zhang, S. Guo, C. Zhao, L. Wang, S. Ma, F. Guan, M. Yao, *Int. J. Biol. Macromol.* **2021**, *187*, 200.
[24] Y. Hu, Y. Jia, S. Wang, Y. Ma, G. Huang, T. Ding, D. Feng, G. M. Genin, Z. Wei, F. Xu, *Adv. Healthcare Mater.* **2023**, *12*, 2201594.
[25] J. Jiang, C. Dai, X. Liu, L. Dai, R. Li, K. Ma, H. Xu, F. Zhao, Z. Zhang, T. He, X. Niu, X. Chen, S. Zhang, *Theranostics* **2021**, *11*, 768.
[26] W. Tang, F. Fang, K. Liu, Z. Huang, H. Li, Y. Yin, J. Wang, G. Wang, L. Wei, Y. Ou, Y. Wang, *ACS Biomater. Sci. Eng.* **2020**, *6*, 2209.
[27] Y. Zheng, G. Wu, L. Chen, Y. Zhang, Y. Luo, Y. Zheng, F. Hu, T. Forouzanfar, H. Lin, B. Liu, *Bioactive Materials* **2021**, *6*, 627.
[28] A. M. Hopkins, E. DeSimone, K. Chwalek, D. L. Kaplan, *Prog. Neurobiol.* **2015**, *125*, 1.
[29] O. O. Ogunshola, *Curr. Pharm. Des.* **2011**, *17*, 2755.
[30] E. Scarian, M. Bordoni, V. Fantini, E. Jacchetti, M. T. Raimondi, L. Diamanti, S. Carelli, C. Cereda, O. Pansarasa, *IJMS* **2022**, *23*, 5344.
[31] I. Matai, G. Kaur, A. Seyedsalehi, A. McClinton, C. T. Laurencin, *Biomaterials* **2020**, *226*, 119536.
[32] L. Ouyang, J. P. Armstrong, Y. Lin, J. P. Wojciechowski, C. Lee-Reeves, D. Hachim, K. Zhou, J. A. Burdick, M. M. Stevens, *Sci. Adv.* **2020**, *6*, eabc5529.
[33] A. Schwab, R. Levato, M. D'Este, S. Piluso, D. Eglin, J. Malda, *Chem. Rev.* **2020**, *120*, 11028.
[34] Q. Gu, E. Tomaskovic-Crook, R. Lozano, Y. Chen, R. M. Kapsa, Q. Zhou, G. G. Wallace, J. M. Crook, *Adv. Healthcare Mater.* **2016**, *5*, 1429.
[35] Y. Song, X. Su, K. F. Firouzian, Y. Fang, T. Zhang, W. Sun, *Biofabrication* **2020**, *12*, 035016.
[36] K. F. Firouzian, Y. Song, F. Lin, T. Zhang, *Biotechnol. Bioeng.* **2020**, *117*, 3094.
[37] Y. Yao, H. A. Coleman, L. Meagher, J. S. Forsythe, H. C. Parkington, *Adv. Healthcare Mater.* **2023**, *12*, 2300801.
[38] J. Kapr, L. Petersilie, T. Distler, I. Lauria, F. Bendt, C. M. Sauter, A. R. Boccaccini, C. R. Rose, E. Fritsche, *Adv. Healthcare Mater.* **2021**, *10*, 2100131.
[39] J. Wang, H. Qiao, Z. Wang, W. Zhao, T. Chen, B. Li, L. Zhu, S. Chen, L. Gu, Y. Wu, Z. Zhang, L. Bi, P. Chen, *Adv. Mater.* **2023**, *35*, 2210631.
[40] D. Joung, V. Truong, C. C. Neitzke, S.-Z. Guo, P. J. Walsh, J. R. Monat, F. Meng, S. H. Park, J. R. Dutton, A. M. Parr, M. C. McAlpine, *Adv. Funct. Mater.* **2018**, *28*, 1801850.
[41] M. Wang, W. Li, J. Hao, A. Gonzales, Z. Zhao, R. S. Flores, X. Kuang, X. Mu, T. Ching, G. Tang, Z. Luo, C. E. Garciamendez-Mijares, J. K. Sahoo, M. F. Wells, G. Niu, P. Agrawal, A. Quiñones-Hinojosa, K. Eggan, Y. S. Zhang, *Nat. Commun.* **2022**, *13*, 3317.
[42] Y. Yan, X. Li, Y. Gao, S. Mathivanan, L. Kong, Y. Tao, Y. Dong, X. Li, A. Bhattacharyya, X. Zhao, S.-C. Zhang, *Cell Stem Cell* **2024**, *31*, 260.
[43] H. Sakai, Y. Fujii, N. Kuwayama, K. Kawaji, Y. Gotoh, Y. Kishi, *Genes Cells* **2019**, *24*, 650.
[44] Y. Zhou, H. Song, G. Ming, *Nat. Rev. Genet.* **2023**, *25*, 26.
[45] X. Qian, Q. Shen, S. K. Goderie, W. He, A. Capela, A. A. Davis, S. Temple, Neuron **2000**, *28*, 69.
[46] V. Braitenberg, A. Schüz, *Cortex: Statistics and Geometry of Neuronal Connectivity*, Springer, Berlin Heidelberg **1998**.
[47] C. Stringer, T. Wang, M. Michaelos, M. Pachitariu, *Nat. Methods* **2021**, *18*, 100.
[48] G. Buzsáki, C. A. Anastassiou, C. Koch, *Nat. Rev. Neurosci.* **2012**, *13*, 407.
[49] T. Sharf, T. van der Molen, S. M. K. Glasauer, E. Guzman, A. P. Buccino, G. Luna, Z. Cheng, M. Audouard, K. G. Ranasinghe, K. Kudo, S. S. Nagarajan, K. R. Tovar, L. R. Petzold, A. Hierlemann, P. K. Hansma, K. S. Kosik, *Nat. Commun.* **2022**, *13*, 4403.
[50] A. Gefen, S. S. Margulies, *J. Biomech.* **2004**, *37*, 1339.
[51] E. Axpe, G. Orive, K. Franze, E. A. Appel, *Nat. Commun.* **2020**, *11*, 3423.
[52] S. K. Seidlits, Z. Z. Khaing, R. R. Petersen, J. D. Nickels, J. E. Vanscoy, J. B. Shear, C. E. Schmidt, *Biomaterials* **2010**, *31*, 3930.
[53] A. K. Ommaya, *J. Biomech.* **1968**, *1*, 127.
[54] J. Weickenmeier, M. Kurt, E. Ozkaya, M. Wintermark, K. B. Pauly, E. Kuhl, *J. Mech. Behav. Biomed. Mater.* **2018**, *77*, 702.
[55] S. Budday, G. Sommer, J. Haybaeck, P. Steinmann, G. A. Holzapfel, E. Kuhl, *Acta Biomater.* **2017**, *60*, 315.
[56] A. J. Thompson, E. K. Pillai, I. B. Dimov, S. K. Foster, C. E. Holt, K. Franze, *eLife* **2019**, *8*, e39356.
[57] L. Z. Shuck, S. H. Advani, *J. Basic Eng-t. Asme.* **1972**, *94*, 905.
[58] A. J. Engler, S. Sen, H. L. Sweeney, D. E. Discher, *Cell* **2006**, *126*, 677.
[59] K. Saha, A. J. Keung, E. F. Irwin, Y. Li, L. Little, D. V. Schaffer, K. E. Healy, *Biophys. J.* **2008**, *95*, 4426.
[60] N. Daviaud, R. H. Friedel, H. Zou, eneuro **2018**, *5*, ENEURO.0219-18.2018.
[61] H. Kleven, I. E. Bjerke, F. Clascá, H. J. Groenewegen, J. G. Bjaalie, T. B. Leergaard, *Nat. Methods* **2023**, *20*, 1822.
[62] S. Budday, E. Kuhl, *Curr. Opin. Biomed. Eng.* **2020**, *15*, 16.